

AstroLoc: Robust Space to Ground Image Localizer

Gabriele Berton

gabriele.berton@polito.it

Alex Stoken

Carlo Masone

Abstract

Astronauts take thousands of photos of Earth per day from the International Space Station, which, once localized on Earth’s surface, are used for a multitude of tasks, ranging from climate change research to disaster management. The localization process, which has been performed manually for decades, has recently been approached through image retrieval solutions: given an astronaut photo, find its most similar match among a large database of geo-tagged satellite images, in a task called Astronaut Photography Localization (APL). Yet, existing APL approaches are trained only using satellite images, without taking advantage of the millions open-source astronaut photos. In this work we present the first APL pipeline capable of leveraging astronaut photos for training. We first produce full localization information for 300,000 manually weakly labeled astronaut photos through an automated pipeline, and then use these images to train a model, called AstroLoc. AstroLoc learns a robust representation of Earth’s surface features through two losses: astronaut photos paired with their matching satellite counterparts in a pairwise loss, and a second loss on clusters of satellite imagery weighted by their relevance to astronaut photography via unsupervised mining. We find that AstroLoc achieves a staggering 35% average improvement in recall@1 over previous SOTA, pushing the limits of existing datasets with a recall@100 consistently over 99%. Finally, we note that AstroLoc, without any fine-tuning, provides excellent results for related tasks like the lost-in-space satellite problem and historical space imagery localization.

1. Introduction

Earth observation is the process of collecting information about the Earth’s surface, which is vital for monitoring the state of our planet. Among the multitude of systems used to acquire Earth observations data, most of which rely on automatic collection by nadir-facing satellites, manual acquisition of photos by astronauts aboard the International Space Station (ISS) is a clear outlier. This imagery has distinctive properties including (1) a wide range of spatial resolutions (up to 2 meters per pixel), (2) the potential for oblique per-

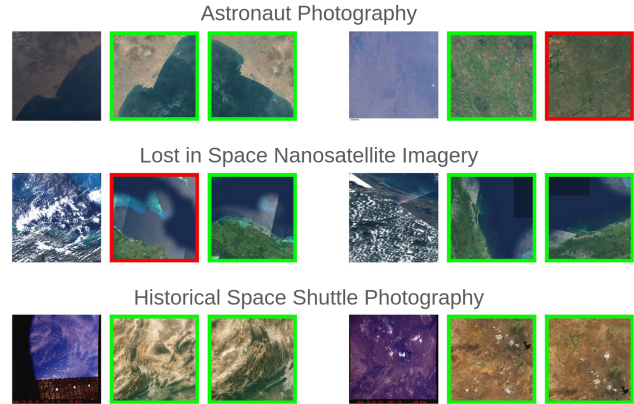


Figure 1. **One model, many space to ground applications.** We train a single model, AstroLoc, that succeeds in multiple space-based image retrieval settings with significant domain gaps. We show strong performance on astronaut photography localization, “lost in space” orbit determination, and historical (Space Shuttle) photography localization. Each group of 3 images represent a query and its top-2 predictions from searching over a worldwide database of thousands of satellite images. Correct predictions in green, wrong predictions in red.

spectives to observe topography and height (*e.g.*, measure the height of a volcanic eruption to divert flights), (3) various illumination conditions (whereas satellite imagery is typically sun-synchronous, always capturing the same area at the same time of day), and (4) offering the highest resolution open source Earth observations data. Furthermore, due to the ISS’s 90 minute repeating orbit, astronauts can be tasked with imaging for near real time disaster response, and they can use human intuition to focus on relevant areas and events, making the photographs very information-dense, whereas satellites commonly collect images of areas regardless of semantic value. All these characteristics make this data source a perfect complement to satellite data and a crucial component for climate science [23], atmospheric phenomena [15, 36], urban planning [8, 13, 26, 29], and, most importantly, disaster management and response [30]¹.

Although over 5 million photos have been collected from the ISS since the beginning of its operations, unfortunately their full potential has yet to be unlocked. The complication

¹<https://storymaps.arcgis.com/stories/947eb734e811465cb0425947b16b62b3>

is that astronaut photos, unlike satellite imagery, are not automatically localized w.r.t. the Earth’s surface. Even though the position of the ISS can be determined from the timestamp of the photo and the ISS orbit path, an astronaut can point their camera (a standard hand-held DSLR) toward any location on Earth within their vast visibility range, which spans roughly 20 million square kilometers (sqkm)². Therefore, localizing a single photo that can cover an area as small as 100 sqkm (*i.e.* 0.0005% of the visible/search area) is akin to finding a needle in a haystack. For example, when an astronaut is above Texas and photographs a wildfire they see, the burning area could be anywhere from Canada to Mexico depending on the camera orientation, and the only way to know where is to geolocate the image.

The potential value these photos hold when geolocated has led to a concerted manual localization effort, with experts and citizen scientists localizing over 300,000 of these images – a process defined by NASA as a “monumentally important, but monumentally time-consuming job”³. Nevertheless, manually geolocating a single astronaut photo can take hours, effectively making this procedure inadequate given the ever-growing number of images that are being collected (up to 10k per day). This problem has prompted recent investigation into automating the task of **Astronaut Photography Localization (APL)** with deep learning models, combining both image retrieval [5] and image matching techniques [4, 32, 33]. Image retrieval is used as a first step, to search within a database of precisely geo-referenced satellite images for those that are most similar to the query astronaut photo. With such a system, a query can be coarsely localized in less than a second, making it a viable solution for such a large scale problem. Afterwards, the retrieval candidates may be refined using more computationally demanding matching techniques. Although these pipelines have shown satisfactory speeds for APL, their performance show a wide margin for improvement, and we hypothesize that this is due to existing APL models being trained with only satellite images [5]. This is a critical limitation, considering that the end goal is to geo-reference astronaut photos, not satellite images.

We argue that it would be beneficial to exploit the available 300,000 hand-labeled open-source astronaut photos to train the image retrieval model. The difficulty with doing so is that these photos are only weakly annotated, *i.e.*, the manual label only provides the GPS location of a random point close to the center of the image. Therefore, these weakly labeled photos cannot be directly used in a metric learning framework, where the model must be provided with pairs of queries (astronaut photos) and database (satellite) images from the same location. In order to meet this criteria, we

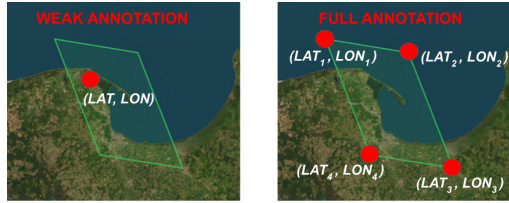


Figure 2. **Visual example of weak (manual) annotation and full annotation of an astronaut photo.** Weak annotation is the GPS coordinates of a single point, which does not provide information regarding the image’s size (*i.e.* it could cover a city or an entire continent), whereas full annotation provides GPS for its 4 corners (called the footprint), from which the coordinate of any pixel within the image can be easily calculated (pixel-wise label).

need these photos to be labeled with their full footprint (*i.e.* precise GPS location of its four corners), so that we can exactly determine images from the database to be used as positive samples (*i.e.*, with a good overlap w.r.t. the training queries). The concept of weak and full labels is visualized in Fig. 2.

In light of these considerations, we first produce a precise annotation of these 300,000 photos, leveraging their weak annotation and a state-of-the-art matching pipeline to label their full footprint. Then, we demonstrate the importance of using this newly annotated data for training, by extending the state-of-the-art method EarthLoc [5] in two ways. First, we create pairs of matching astronaut-satellite images, and use them in a pairwise contrastive loss that takes advantage of the fact that the two images within each pair come from different domains. The creation of these pairs relies on the new annotation, *i.e.*, we select a pair if the two images have enough intersection over union on Earth’s surface. Even with this loss that takes advantage of the newly labeled 300,000 astronaut photos, it is still important to fully leverage the much larger set of 5.3M geo-referenced satellite images, as is done in previous methods. However, we observe that the satellite images are uniformly distributed on the surface of the Earth, whereas the photos from astronauts tend to be unevenly distributed, with higher concentrations in salient areas like volcanoes, glaciers, lakes and coastlines. Therefore, we use a second contrastive loss that leverages tuples of satellite images only, but sampled according to the distribution of astronaut photos.

We find that our training pipeline, yielding a model we call **AstroLoc**, leads to a model so powerful that it saturates existing test sets (recall@100 above 99%), and we therefore propose new, more challenging test sets that better reflect the task of APL in the real world.

To summarize, our contributions are as follows:

- we provide precise localization labels to 300,000 weakly labeled astronaut photographs, which will be made available to support further research in this field;
- we propose two techniques to effectively adopt this data

²Considering that the ISS orbits at an altitude of 415 kilometers.

³We highly encourage the reader to view this clip https://www.youtube.com/watch?v=drpP_Iss0gA&t=295s

source into an Astronaut Photography Localization training pipeline;

- AstroLoc leads to a staggering 35% improvement on average of recall@1 over previous SOTA, and practically solves existing test sets (recall@100 around 99%);

Furthermore, AstroLoc is practically useful and has already been used to localize hundreds of thousand of images available here⁴, and shows great potential for tasks like the lost-in-space satellite and historical space image localization. We finally note that, thanks to AstroLoc, in a few months the backlog of non-localized astronaut photos will be nearly empty for the first time since the launch of the ISS, with the exception of a small fraction that still produce failure cases.

2. Related Work

Astronaut and satellite imagery localization The task of localizing photos taken from Earth’s orbit has been studied in a number of domains. Straub and Christian [34] examine the possibility of matching the coastline of imagery from satellites to enhance their autonomous navigation capabilities. Schockley and Bettinger [27] take a similar approach, but instead propose using terrestrial illumination matching. The problem is more recently addressed by McCleary et al. [20], which selects a set of landmarks on Earth to achieve the same goal. They note that common hardware solutions for localization are expensive (~10k\$) for nanosatellite developers, making a software solution a game changer for the industry. For the similar task of localizing astronaut photography, which was historically performed by hand [32], Stoken and Fisher proposed an automated solution leveraging image matching [32], in a framework that was then expanded to localize night-time imagery [33].

While these solutions have advanced the field of Earth from space localization, they are limited, as Berton et al. [5] notes. The matching-based methods can not achieve the scalability and speed required to localize astronaut photographs in real time. Berton et al. proposes approaching the task as an image retrieval problem, where the database is composed of satellite images of known location. In this setting, AnyLoc [17], a universal place recognition model, has been shown to produce strong performance and robustness to the query-database domain gap.

Unmanned aerial vehicle localization A closely related task is that of unmanned aerial vehicle (UAV) localization. Similar to Astronaut Photography Localization (APL), it is approached through cross-domain image retrieval, where the database is often made of satellite imagery and the queries are photos collected by a drone. The goal is to efficiently find the best prediction for a given query in order to localize the drone in real time [38]. Among no-

⁴Photos available at: <https://eol.jsc.nasa.gov/ExplorePhotos/>

Type	Queries	Database
Acquisition	manual, by astronauts	automatic, by satellites
Number (Annotation)	5M (none), 300k (weak)	5.2M (full)
Extent	40 to 1,357,493 sqkm	346 to 391,776 sqkm
Extent percentile (5 / 95)	239 / 39,729 sqkm	465 / 16,026 sqkm
Occlusions	Yes (ISS hardware, clouds)	No
Obliquity & distortion	Yes	No
Illumination changes	Yes (e.g. day/dawn/sunset)	No
Years	2000 to 2024	2018 to 2021
Source	https://eol.jsc.nasa.gov/	https://s2maps.eu
Coverage	scattered, biased on glaciers, volcanoes etc.	dense, worldwide

Table 1. **Overview of data.** Information reported about satellite imagery refers specifically to the data used in this project, not satellite imagery in general. The labeling refers to the weak and full labeling shown in Fig. 2.

table examples from the literature, Bianchi and Barfoot [6] introduced a method utilizing autoencoded satellite images, significantly reducing storage and computation costs while maintaining robust localization performance. Dai et al. [7] proposed an end-to-end framework, FPI, that directly identifies UAV locations by matching UAV-view images with satellite-view counterparts, streamlining the localization process. Li et al. [18] developed a transformer-based adaptive semantic aggregation method, focusing on part-level representations to improve UAV-satellite image matching by capturing detailed semantic information.

Further improvements in UAV localization are achieved by orientation-guided methods, as shown by Deuser et al. [10], who use orientation-guided contrastive learning to improve UAV-satellite image alignment. Zhu et al. [39] proposed a modern backbone architecture optimized for efficient UAV geo-localization, enhancing both speed and accuracy for UAV applications.

3. Data

Our goal is to localize the extent of **astronaut photos (queries)** given a worldwide map of geo-referenced **satellite images (database)**. Astronaut photographs represent one of the most diverse and long standing Earth observations data sources. The dataset contains a wide range in spatial resolution, field of view, illumination (including night imagery), and obliquity (astronauts can tilt the camera and take oblique photos). These images have many applications in numerous fields [8, 13, 15, 23, 26, 29, 36], and most importantly in disaster management and response [30]⁵.

For database images we follow [5] and use a *composited* set of cloudless open-source satellite yearly imagery from Sentinel-2, named S2. We use tiles from zoom levels 8-12 [24] (expanding in both directions on the set used in [5]), to provide a thorough train and test set that reflects the extents of the query images. Characteristics of astronaut and satellite imagery are compared in Tab. 1.

⁵<https://eol.jsc.nasa.gov/Collections/Disasters/ShowDisastersCollection.pl>

3.1. Training Set

In contrast to previous work, we propose taking advantage of the 300k manually localized astronaut photos for training. The idea is to pair these photos with matching satellite imagery from the database (*i.e.* with enough Intersection over Union, or IoU) and apply contrastive training to train models that are robust to the domain differences between astronaut and satellite imagery. Unfortunately, the available manual localization is only a weak annotation (see Fig. 2), which does not provide enough information to compute IoU. To overcome this limitation, we estimate the precise footprint for each query image. For each manually localized query, we select as potential positives all the database images which contain the weak label point at each zoom level, and we rotate these potential positives by 90° , 180° and 270° to maximize the chance of finding a similar image among the potential positives. In practice, given five zoom levels, four rotations, and the fact that each point is covered by four images (there is overlap among the tiles), there are $5 \times 4 \times 4 = 80$ potential positives per query. Note that different zoom levels are required because it is impossible to estimate an image extent with only a weak label, and a photo could cover an area as small as a city or as big as a continent. We then perform image matching with SuperPoint [9] + LightGlue [19] and the EarthMatch pipeline [4] to get the footprint coordinates of each query.

This localization was successful for 221k queries, with the remaining ones not localizable due to either errors in manual labeling, too much obstruction from clouds, or the image being of the horizon (*i.e.* Earth limb photograph, with two corners representing outer space, hence an invalid footprint). With this now precisely localized collection of astronaut photography, we pair each query with the all database images with an IoU over $t_{iou} = 0.2$ producing 865k query-database training pairs. We then discard any pair containing a query that is included within the test sets to avoid any data leakage.

3.2. Evaluation Sets

Evaluation sets are made of queries and the associated database to localize them. Six evaluation sets were proposed in [5], covering geographical areas across five continents that mirror astronaut photography use cases like land change study and flood monitoring. However, as detailed in their limitations [5], the test sets only contain queries whose projected area on Earth’s surface is between 5,000 and 900,000 sq km, which represents only 22% of all astronaut photo queries, as shown in Fig. 3.

We therefore propose new evaluation sets, to include all available geolocated queries within an evaluation area, as well as add zoom levels 8 and 12 to the database to match the wider range of query areas. To avoid introducing complexity, we use the same regions as the test sets from [5].

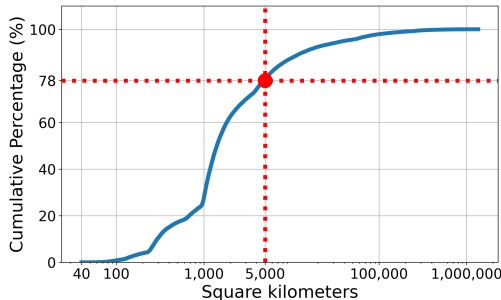


Figure 3. **Distribution of queries by covered area.** The red mark at 5,000 sqkm shows that 78% of astronaut photographs cover an area lower than 5,000 sqkm. Thus, the test sets in Tab. 2 do not contain this vast majority of queries, leading us to propose test sets containing all queries used for experiments in Tab. 3.

These datasets were named after the geographic location of their center, like Texas, Gobi, and Amazon, so we call these new extended versions Texas-L (L for Large), Gobi-L, etc.

4. Method

4.1. Setting

Task Astronaut Photography Localization (APL) is the task of estimating the geographic location covered by a photo (query) taken by astronauts. APL can be approached through image retrieval: for each query, estimate its location by finding the most similar match in a large database of geolocated images of Earth.

Formalization We pose the task as a retrieval problem, and rely on three sets of images:

- The **database** $\mathcal{D} = \{d_1, d_2, \dots, d_{N_{\mathcal{D}}}\}$ is a set of $N_{\mathcal{D}}$ satellite images, each characterized by their RGB content and the coordinate label of their four corners, called the *footprint*. Formally, the footprint for a generic image $d_i \in \mathcal{D}$ is denoted as $F_i = \{lat_1, lon_1, lat_2, lon_2, lat_3, lon_3, lat_4, lon_4\}$ where lon_k and lat_k denote the longitude and latitude of the k -th corner, respectively (Fig. 2).
- The **training queries** $\mathcal{Q} = \{q_1, q_2, \dots, q_{N_{\mathcal{Q}}}\}$ is a set of $N_{\mathcal{Q}}$ astronaut photos, with RGB content and footprints (localized as explained in Sec. 3.1).
- The **test queries** $\mathcal{T} = \{t_1, t_2, \dots, t_{N_{\mathcal{T}}}\}$ is another set of $N_{\mathcal{T}}$ astronaut photos, disjoint from \mathcal{Q} , each characterized by its RGB content and timestamp. The timestamp is crucial in determining the location of the ISS when the photo was taken, which enables narrowing down the search space from a world-wide area (510M sqkm) to the local area visible from the ISS at that time (20M sqkm). Note that due to cosmic radiation bit flips, the timestamp can sometimes be incorrect: in such cases, it is necessary to conduct a “world-wide” search (see Sec. 5.5).

Training with Astronaut Photos (Queries) While vari-

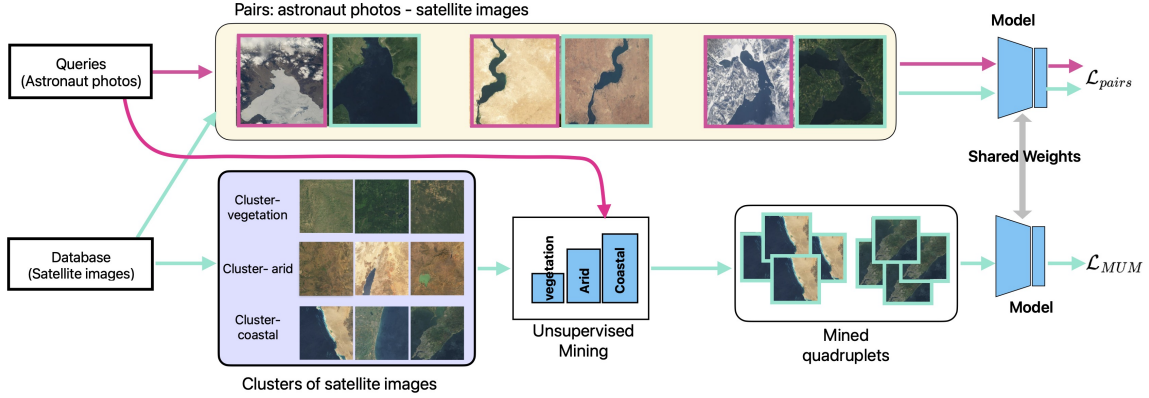


Figure 4. **Overview of AstroLoc training pipeline.** The upper branch feeds pairs of matching query-database images to the pairwise loss (Sec. 4.2). The lower branch (Sec. 4.3) first creates clusters of satellite images, then queries are assigned to these clusters, and then the clusters are sampled according to how many queries are assigned to each cluster (unsupervised mining). A training batch (mined quadruplets, *i.e.* tuples of 4 images) is sampled from a single cluster, and fed to the Multi-similarity Unsupervised Mining (MUM) loss. Queries are not fed to the MUM loss, and are not used to compute the clusters — they are only used to sample training data from a closer distribution to the queries’.

ous approaches have been used for APL, no previous work has taken advantage of the huge dataset of 300k astronaut photos labeled by human experts. We argue that their use at training time can lead to huge improvements in performance, and we present two novel techniques to use this data. In Sec. 4.2 we show how we use pairs of matching query-reference images (*i.e.*, depicting the same location) described in Sec. 3.1 to implement a *pairwise loss* for this setup (see Fig. 4 top). Additionally, we also use a second loss computed on tuples of satellite images, by sampling them using the distribution of the queries (see an overview in Fig. 4 bottom), allowing us to use the entire set of database images for training (whereas the *pairwise loss* can be applied only on areas covered by astronaut photos) while still leveraging the queries, as we explain in Sec. 4.3.

4.2. Query-Satellite Pairwise Loss

Given the cross-domain nature of the problem, we aim to take matching images from the different distributions and applying contrastive learning to encode their relationship in the feature space. To this end, we create a batch $\mathcal{P} = \{p_1, p_2, \dots, p_B\}$ of query-database pairs $p_i = (q_i, d_i) \in (\mathcal{Q}, \mathcal{D})$ that have an intersection over union (IoU) higher than a threshold t_{iou} ⁶ (see examples in Fig. 4 top). We ensure that within a batch there are no two pairs that have geographic overlap, so that for a pair $p_i \in \mathcal{P}$ all the images from other pairs $p_j \in \mathcal{P} \setminus \{p_i\}$ are negative examples.

With this setting, we define a contrastive loss that comprises two terms: an attraction term \mathcal{L}_{pos} that acts between

images in a matching pair, pulling their representations closer, and a repulsion term \mathcal{L}_{neg} , that is applied between images from different pairs (*i.e.*, non matching), pushing them apart. Formally, given a similarity measure $\mathcal{S}(I_1, I_2)$ between the features of two image (*e.g.*, the cosine similarity), we define the positive loss term as

$$\mathcal{L}_{pos} = \frac{1}{\alpha_1 B} \sum_{i=1}^B \gamma(\alpha_1, q_i, d_i) \quad (1)$$

where $\alpha_1 > 0$ is a gain and

$$\gamma(x, y, z) = \log \left[1 + e^{-x \times \mathcal{S}(y, z)} \right] \quad (2)$$

is the attraction function.

For the negative loss term, let us first denote with $\mathcal{P}_Q = \{q_1, q_2, \dots, q_B\}$ the set of all queries in the batch \mathcal{P} , and with $\mathcal{P}_D = \{d_1, d_2, \dots, d_B\}$ the set of all database images in \mathcal{P} . With this notation, we define \mathcal{L}_{neg} as

$$\begin{aligned} \mathcal{L}_{neg} = \frac{1}{\beta_1 B} \sum_{i=1}^B & \left[\varphi(\beta_1, q_i, \mathcal{P}_Q \setminus \{q_i\}) + \varphi(\beta_1, q_i, \mathcal{P}_D \setminus \{d_i\}) \right. \\ & \left. + \varphi(\beta_1, d_i, \mathcal{P}_Q \setminus \{q_i\}) + \varphi(\beta_1, d_i, \mathcal{P}_D \setminus \{d_i\}) \right] \end{aligned} \quad (3)$$

where $\beta_1 > 0$ is a gain and

$$\varphi(x, y, \mathcal{Z}) = \log \left(1 + \sum_{j=1}^{|\mathcal{Z}|} e^{x \times \mathcal{S}(y, z_j)} \right) \quad (4)$$

is the repulsion function. The overall loss is

$$\mathcal{L}_{pairs} = \mathcal{L}_{pos} + \mathcal{L}_{neg} \quad (5)$$

⁶For the sake of readability, we abused the notation by implying that a matching query and database images from the sets \mathcal{Q} and \mathcal{D} have the same index as the index of the pair they belong to. This trick to simplify the notation is equivalent to have preliminarily sorted the sets \mathcal{Q} and \mathcal{D} .

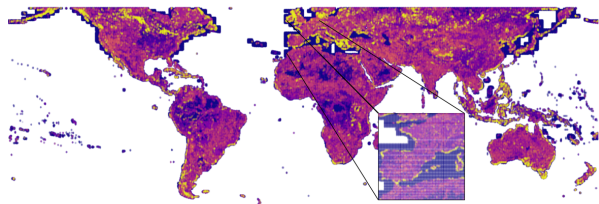


Figure 5. **Weighted clusters from unsupervised mining.** The spatial distribution of images from 50 mined clusters, colored by cluster sampling weight. Higher weighted areas (yellow) are sampled more frequently than lower weighted areas (blue).

4.3. Unsupervised Mining

To fully exploit the much larger corpus of satellite image, we use a second loss inspired by EarthLoc [5], where quadruplets of satellite images are used with a multi-similarity loss [35] to learn robust feature representations. Each quadruplet contains four images of the same place, *i.e.* positives toward each other, and negatives w.r.t. the images from other quadruplets. To implement this idea, EarthLoc [5] first uses an offline clustering strategy, to divide the database images into visually similar subsets (*e.g.*, a cluster with images of mountains, one with deserts, one with coastlines, etc.). Formally, it creates a set of K clusters $\mathcal{C}_1, \dots, \mathcal{C}_K$ such that

$$\bigcup_{k=1}^K \mathcal{C}_k = \mathcal{D} \quad (6)$$

The clusters are computed with a k-means algorithm using features computed with the model while it’s training, as common practice with mining techniques [2]. Then, at each iteration a batch of quadruplets from one single cluster is created, where the chosen cluster is uniformly sampled among all possible clusters. Formally, we denote this sampled batch of quadruplets as

$$\mathcal{H}_k = \{h_1, \dots, h_H\} \quad (7)$$

where the generic $h_i = (h_{i_1}, \dots, h_{i_4}) \in (\mathcal{C}_k, \mathcal{C}_k, \mathcal{C}_k, \mathcal{C}_k)$ is a quadruplet of images from the same location, and the cluster is chosen according to uniform sampling

$$k \sim U(1, K) \quad (8)$$

EarthLoc demonstrates that this random sampling of clusters achieves significant improvement over sampling quadruplets from the entire database \mathcal{D} . This is because clustering ensures that all the images in the batch, including the ones used as negatives, are visually similar, thus yielding a better signal for a contrastive loss (*i.e.* that the negatives are harder negatives). However, we argue that the uniform sampling in Eq. (8) leads the model to learn on a data distribution that is geographically very dissimilar from how the photos from astronauts are distributed. Generally, astronauts take few photos of feature-less landscapes like deserts and ice sheets, while often photographing scenes relevant to natural disasters and climate change like glaciers, coastlines and islands. To avoid this distribution shift, we pro-

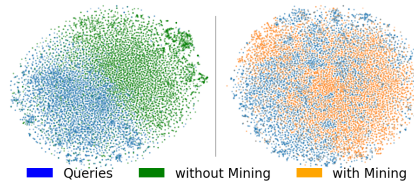


Figure 6. **t-SNE plot of features with and without our mining.** Blue dots represent query set features, and other dots represent features of the training quadruplets (made of database images) with and without our mining, (right and left, respectively). Although neither is a perfect blend, our mining allows sampling from a distribution much more intertwined with the query distribution.

pose sampling the cluster to be used to create the batch \mathcal{H}_k according to the distribution of the query set \mathcal{Q} . We first compute the features from our training queries, assign them to clusters, and then apply a *weighted* sampling of the clusters weighted by how many queries belong to it. Note that the clusters are computed only on the database, and the queries are simply assigned to them to determine the clusters’ weighting. For example, if there are three clusters A, B and C (see Fig. 4), and 10% of queries are assigned to cluster A, 90% to cluster B, and 0 to cluster C, then the training batches will be sampled 10% from cluster A and 90% from cluster B (see Fig. 4). Formally, let’s denote with b_1, \dots, b_K the size of the bins derived from assigning the features of the training queries to the K clusters. The sampling of the cluster is then replaced by

$$k \sim B(Q, 1, k) \quad (9)$$

where B denotes the weighted distribution according to the bins b_1, \dots, b_K , *i.e.* such that

$$Pr(k) = \frac{b_k}{\sum_{i=1}^K b_i} \quad (10)$$

Unlike what commonly done in contrastive learning [1, 2, 21, 22], this mining is unsupervised, as the queries’ labels are not used, meaning that we could potentially use all of the 5M existing astronaut photos. In practice we use only training queries to avoid seeing test queries at train time. The second loss used in our pipeline is thus

$$\mathcal{L}_{MUM} = \frac{1}{4H} \sum_{i=1}^H \left[\frac{1}{\alpha_2} \sum_{j=1}^4 \log \left(1 + \sum_{d \in \mathcal{H}_i \setminus \{h_{i_j}\}} e^{-\alpha_2 \mathcal{S}(h_{i_j}, d)} \right) + \frac{1}{\beta_2} \sum_{j=1}^4 \log \left(1 + \sum_{d \in \mathcal{H}_k \setminus \{h_i\}} e^{+\beta_2 \mathcal{S}(h_{i_j}, d)} \right) \right] \quad (11)$$

where k is sampled according to Eq. (9), α_2 and β_2 are positive hyperparameters, and MUM stands for **M**ulti-similarity with **U**nsupervised **M**ining.

To summarize, our unsupervised mining relies on the following steps:

1. extract features from database (*i.e.* satellite imagery);

2. compute k-means clustering on these features;
3. extract features from training queries (*i.e.* astronaut photos), assign them to the clusters;
4. sample database images in proportion to the number of training queries assigned to that cluster.

These steps are repeated periodically every 5000 iterations, increasing training time by less than 10%. This is a data-driven unsupervised mining, where the goal is to sample database images using the training queries distribution (defined in eq. 9). The practical effect of this mining is visible in Fig. 5, where yellower areas represent more informative clusters that are therefore sampled more often.

Finally, our final loss is the sum of the two losses:

$$\mathcal{L} = \lambda_1 \mathcal{L}_{pairs} + \lambda_2 \mathcal{L}_{MUM} \quad (12)$$

5. Experiments

5.1. Implementation Details

Training We set the hyperparameters as follows: $t_{iou} = 0.2$, $\alpha_1 = 1$, $\alpha_2 = 1$, $\beta_1 = 50$, $\beta_2 = 50$, $\lambda_1 = 1$, $\lambda_2 = 1$, $K = 50$, batch size = 48 (48 pairs for pair loss, 48 quadruplets for MUM loss), learning rate = $5e-5$, Adam optimizer. We use as architecture a DINO-v2-base backbone [25] with SALAD [14] and a linear layer to reduce feature dimensionality (from 8448 to 2048) (*i.e.* a similar model to AnyLoc [17] while being over 10 times lighter as they use DINO-v2-giant). Training runs for 30k iterations. As in [5], the Texas dataset is used as validation.

Evaluation We follow common procedure [5] by doing image retrieval with an augmented dataset (*i.e.* applying four 90° rotations to each image), and using as metric the recall@N, as the percentage of queries where at least one of the top-N predictions is a correct match to the query.

5.2. Results

In Tab. 2 we report experiments on the test sets proposed by [5]. For fairness, we include results with a more powerful version of EarthLoc that uses the same architecture and training data of AstroLoc, which we refer to as EarthLoc++.

Results clearly show that, whereas previously there was no dominant method between EarthLoc and AnyLoc, the introduction of AstroLoc provides a new state-of-the-art model which significantly outperforms all previous, achieving a near perfect (above 99%) recall@100 on all six evaluation sets. Note that the recall@100 is more relevant in the real world than recall@1, since it is common practice to re-rank the top-N predictions with image matching methods [4, 32]. Some qualitative results of queries and their predictions are in Fig. 1, with many more in the supplementary.

New test sets Here we compute experiments on the newly extended test sets described in Sec. 3.2, which provide a

setting that is more similar to the real world scenario and more challenging. Results, reported in Tab. 3, illustrate that AstroLoc is able to outperform previous models by an even wider margin, and presents recall@100 consistently above 96% even in these more comprehensive and complex cases.

5.3. Other Space to Ground Use Cases

In this paper we test the robustness of AstroLoc by performing experiments on two related tasks: the lost-in-space problem and historical space imagery localization. Given the lack of space, we present a thorough explanation of the tasks, motivations, experimental details and results in the supplementary, while only offering a brief summary here.

The Lost-in-Space satellite problem has the goal of identifying the location/orbit of nanosatellites through computer vision [20], requiring photos be searched for over the entire planet. We use as queries the images from McLeary et al. [20], and a worldwide database at zoom level 9 (12k images). Results in Tab. 4 highlight the robustness and adaptability of AstroLoc, which is the only method to achieve a R@1 over 50% on the retrieval-formulation of lost in space, outperforming all other methods by at least 45% of R@1.

Historical space imagery localization Historical imagery of Earth from space is a unique source of data to understand how Earth has changed over decadal time spans. We perform experiments on 704 queries from early Space Shuttle days (1981-1984), on a worldwide database, and report results in Tab. 5. We empirically find that AstroLoc achieves strong results even on these old photographs, showcasing its robustness to various types of domain changes.

5.4. Ablations

Training setup We compute ablations on the losses and mining in Tab. 6, where results clearly show the strong impact from each module in our pipeline. Most importantly, the combination of these components presents the optimal characteristic of orthogonality, in that their mixture has notably higher results than each of the singular elements. Features visualizations of the model trained with and without our mining is also shown in Fig. 6.

Feature dimensionality Given that feature dimensionality plays a crucial role in any large-scale retrieval task, as it is linearly correlated with the test-time memory footprint and matching time (*i.e.* the time it takes to process the kNN), we present a plot (Fig. 7) of how results vary when changing the dimension, as we compute results with two versions of the DINO-v2 backbone, base and small. Interestingly, we find that results increase up to the highest dimensionality (*i.e.* 8448, equal to the input dimension to the final linear layer), showing no plateau at lower dimensions.

Method	Texas (6k / 34k)			Alps (2k / 53k)			California (4k / 30k)			Gobi Desert (1k / 54k)			Amazon (1k / 19k)			Toshka Lakes (2k / 63k)		
	R@1	R@10	R@100	R@1	R@10	R@100	R@1	R@10	R@100	R@1	R@10	R@100	R@1	R@10	R@100	R@1	R@10	R@100
Nadir	2.4	-	-	1.2	-	-	2.4	-	-	1.8	-	-	3.1	-	-	1.4	-	-
Random Choice	0.2	1.7	15.5	0.1	1.1	11.6	0.2	2.3	20.1	0.1	1.0	13.2	0.1	1.1	11.5	0.2	1.2	9.1
TorchGeo [31] (SSL w SeCo [37])	6.1	15.6	41.7	7.4	20.2	49.2	5.1	14.5	37.1	3.7	14.0	38.9	4.6	13.3	32.9	5.7	15.6	38.5
TorchGeo [31] (SSL w GASSL [3])	9.7	22.8	46.4	9.1	23.1	50.5	13.3	31.4	58.8	6.3	17.5	45.4	8.3	20.3	40.1	20.4	38.6	64.2
OGCL UAV-View [10] [11]	17.6	33.2	55.9	14.6	33.2	63.9	22.8	48.1	74.9	7.6	22.8	50.1	20.4	39.1	62.5	31.8	51.8	74.4
MBEG [39]	7.0	17.6	35.1	6.6	19.3	45.9	8.7	20.7	41.5	4.4	15.0	38.0	6.4	17.1	39.3	8.1	20.7	49.1
AnyLoc [17]	44.1	68.7	87.8	40.7	70.8	92.0	48.7	75.0	91.6	28.7	57.0	81.7	38.6	63.8	86.2	63.7	84.5	96.3
EarthLoc [5]	55.9	73.0	88.3	58.4	76.8	89.5	58.0	76.0	91.4	51.1	67.5	86.5	47.2	67.9	84.6	72.2	85.0	93.3
EarthLoc++ [5]	80.0	89.4	95.9	80.6	91.2	96.7	82.9	92.0	97.9	67.6	84.6	94.6	73.6	85.5	93.1	90.1	95.3	98.2
AstroLoc	96.1	98.7	99.7	98.1	99.5	99.8	97.4	99.2	99.8	94.6	99.2	99.9	93.0	96.9	99.1	99.0	99.6	99.9

Table 2. **Recalls on APL test sets from EarthLoc [5]**, from which we source most of the numbers in the table. AstroLoc comfortably and consistently achieves recall over 90%, outperforming all other methods by a large margin. Numbers next to each test set name (e.g. Texas 6k / 34k) represent number of queries / database images. R@N indicates the recall-at-N. Best results **bold**, second best underlined.

Method	Features dimension	Memory (GB)	Total latency (hh:mm)	Per query latency (ms)	Texas-L (21k / 179k)		Alps-L (10k / 261k)		California-L (12k / 166k)		Gobi Desert-L (2k / 284k)		Amazon-L (3k / 101k)		Toshka Lakes-L (9k / 299k)	
					R@1	@100	R@1	@100	R@1	@100	R@1	@100	R@1	@100	R@1	@100
AnyLoc	49152	235 GB	23:51	291	29.2	72.2	30.9	78.9	31.7	76.3	22.9	68.2	20.4	63.5	34.9	76.8
EarthLoc	4096	19 GB	1:12	21	44.0	75.0	52.9	82.6	49.1	80.4	33.9	70.1	34.9	70.6	63.3	86.5
EarthLoc++	2048	9 GB	1:42	12	72.4	91.5	79.4	94.7	75.4	92.9	62.6	87.2	62.6	89.2	83.4	95.1
AstroLoc	2048	9 GB	1:42	12	91.1	98.5	94.6	99.2	92.1	98.7	84.2	96.2	83.8	96.8	94.8	99.0

Table 3. **Results on our extended versions of the test sets from Tab. 2.** “-L” (for “large”) test sets better represent the performance that an APL model would achieve if deployed, as no filtering has been applied on test queries. The two numbers (e.g. Texas 21k / 179k) represent the number of queries and database images. *Memory*, *Total latency* and *Per query latency* refer to testing on the Texas dataset. *Memory* is the memory required to store features; *Total latency* is the time to run the test (including database feature extraction); and *Per query latency* is the time needed to localize one query, which consists of query feature extraction and kNN search (kNN is the primary bottleneck). All tests are performed with an A100 and a 32-core CPU, using FAISS [12] for efficient kNN.

Method	# Params (M)	R@1	R@5	R@10	R@20	R@100
AnyLoc	1136	4.4	9.6	13.4	19.0	40.0
EarthLoc	<u>27.6</u>	3.3	7.0	8.8	12.0	27.6
AstroLoc	105	52.7	63.9	68.7	73.3	83.7
AstroLoc-tiny	27.2	<u>36.7</u>	<u>49.4</u>	<u>55.3</u>	<u>61.6</u>	<u>74.5</u>

Table 4. **Results of Lost-in-Space satellite problem.** Using the dataset from VINSat [20] as queries, we show AstroLoc can also achieve good results on this additional task. AstroLoc-tiny is a tiny version more suitable for deployment on a nanosatellite, with 27M model parameters and 512 dimensional features.

Method	R@1	R@5	R@10	R@20	R@100
AnyLoc	19.6	32.7	40.5	47.2	<u>65.2</u>
EarthLoc	<u>29.5</u>	<u>40.1</u>	<u>43.5</u>	<u>48.7</u>	64.5
AstroLoc	82.0	89.9	91.9	94.2	96.7

Table 5. **Results on historical imagery localization.** The 704 queries are 40 year-old photos from the early days of the Space Shuttle. Searched is conducted across the whole globe.

Method	Texas-L			Alps-L			California-L		
	R@1	R@10	R@100	R@1	R@10	R@100	R@1	R@10	R@100
Pair Loss	83.6	93.1	97.5	87.2	95.0	98.2	85.8	93.7	97.8
MS loss (default mining)	72.4	83.3	91.5	79.4	89.1	94.7	75.4	85.5	92.9
MUM loss	82.2	91.1	97.1	86.9	94.5	97.9	84.1	93.0	97.8
Pair Loss + MS loss	86.5	94.1	97.7	91.5	96.5	98.6	87.8	94.6	97.9
AstroLoc: Pair Loss + MUM loss	91.1	96.2	98.5	94.6	97.8	99.2	92.1	96.7	98.7

Table 6. **Ablations on training setup.** We show results using different loss formulations (only pair/MS/MUM, and combinations of these) and then the final complete architecture, AstroLoc, comprising the pair loss and MUM loss.

5.5. Toward Worldwide Search

Astronaut photographs are associated with a timestamp which, combined with the known orbit of the ISS, can be used to obtain the position of the camera when the photo was taken, allowing the search space to be reduced from the entire extent of the Earth to just 20M sqkm (the area

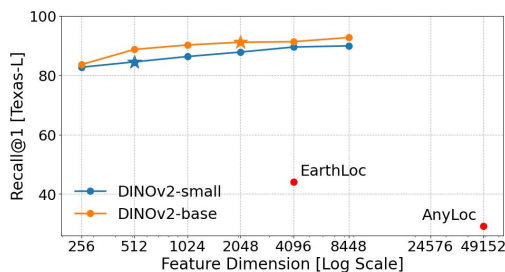


Figure 7. **Ablation on feature size.** Backbone (DINO-v2 small/base) with different feature size/dimension. Stars are models selected for our experiments, blue is AstroLoc-tiny (Sec. 5.3) and orange is AstroLoc in all other tables. R@1 computed on Texas-L.

Method	R@1	R@5	R@10	R@20	R@100
EarthLoc	40.3	49.5	53.2	57.1	66.6
AstroLoc	86.9	91.9	93.4	94.6	96.8

Table 7. **World-wide search.** Using the same query sets as Tab. 3, but with a database encompassing the entire Earth. Results computed for the best performing methods only, except AnyLoc [17], due to its large features (49,152-D vs EarthLoc’s 4096-D) requiring 600GB of RAM to store features to compute kNN.

of Earth’s surface visible from the ISS). However, due to high-energy cosmic particles causing bit-flips in cameras, the timestamp can be unreliable, leaving no information about which area of the Earth the photo is taken near.

We therefore propose the task of worldwide astronaut photography localization, where the database covers the entire world with 881k images. Results (Tab. 7) show that AstroLoc achieves a recall@100 of 96.8%, proving its robustness even in this highly challenging scenario.

6. Conclusions

We tackle the task of Astronaut Photography Localization (APL), obtaining a robust APL model by leveraging a huge set of weakly annotated astronaut photographs, for which we first computed full localization labels. We propose two ways to enhance our model through this data, first adopting them (paired with their satellite counterparts) in an ad-hoc pairwise loss, and second using them to mine ideal training data to pass to our model. We thus obtain a new model, AstroLoc, which shows impressive results on all APL datasets; furthermore, we find that AstroLoc can be utilized in other related tasks, like the lost-in-space problem and the localization of historical space imagery. Finally, we note that we have already used AstroLoc (in conjunction with EarthMatch’s post-processing) to provide localization for a staggering 500k photos, and anticipate that in a few months the backlog of non-localized photos will be nearly empty for the first time since the launch of the ISS.

Acknowledgements. We acknowledge the Cineca award under the Iskra initiative, for the availability of high performance computing resources. This work was supported by CINI. Project supported by ESA Network of Resources Initiative. This study was carried out within the project FAIR - Future Artificial Intelligence Research - and received funding from the European Union Next-GenerationEU (Piano nazionale di ripresa e resilienza (PNRR) – missione 4 componente 2, investimento 1.3 – D.D. 1555 11/10/2022, PE00000013). This manuscript reflects only the authors’ views and opinions, neither the European Union nor the European Commission can be considered responsible for them. European Lighthouse on Secure and Safe AI – ELSA, Horizon EU Grant ID: 101070617

References

- [1] Amar Ali-Bey, Brahim Chaib-draa, and Philippe Giguere. Global proxy-based hard mining for visual place recognition. In *33rd British Machine Vision Conference 2022, BMVC 2022, London, UK, November 21-24, 2022*. BMVA Press, 2022. 6
- [2] Relja Arandjelović, Petr Gronat, Akihiko Torii, Tomas Pajdla, and Josef Sivic. NetVLAD: CNN architecture for weakly supervised place recognition. *IEEE Transactions on Pattern Analysis and Machine Intelligence*, 40(6):1437–1451, 2018. 6
- [3] Kumar Ayush, Burak Uzkent, Chenlin Meng, Kumar Tanmay, Marshall Burke, David Lobell, and Stefano Ermon. Geography-aware self-supervised learning. *IEEE International Conference on Computer Vision*, 2021. 8
- [4] Gabriele Berton, Gabriele Goletto, Gabriele Trivigno, Alex Stoken, Barbara Caputo, and Carlo Masone. Earthmatch: Iterative coregistration for fine-grained localization of astronaut photography. In *Proceedings of the IEEE/CVF Conference on Computer Vision and Pattern Recognition (CVPR) Workshops*, 2024. 2, 4, 7
- [5] Gabriele Berton, Alex Stoken, Barbara Caputo, and Carlo Masone. Earthloc: Astronaut photography localization by indexing earth from space. In *IEEE Conference on Computer Vision and Pattern Recognition*, 2024. 2, 3, 4, 6, 7, 8
- [6] Mollie Bianchi and Timothy D. Barfoot. Uav localization using autoencoded satellite images. *arXiv preprint arXiv:2102.05692*, 2021. 3
- [7] Ming Dai, Enhui Zheng, Zhenhua Feng, Jiahao Chen, and Wankou Yang. Finding point with image: A simple and efficient method for uav self-localization. *arXiv preprint arXiv:2208.06561*, 2022. 3
- [8] Alejandro Sánchez de Miguel, Jonathan Bennie, Emma Rosenfeld, Simon Dzurjak, and Kevin J. Gaston. Environmental risks from artificial nighttime lighting widespread and increasing across europe. *Science Advances*, 8(37): eabl6891, 2022. 1, 3
- [9] Daniel DeTone, Tomasz Malisiewicz, and Andrew Rabinovich. Superpoint: Self-supervised interest point detection and description. In *Proceedings of the IEEE conference on computer vision and pattern recognition workshops*, pages 224–236, 2018. 4
- [10] Fabian Deuser, Konrad Habel, Martin Werner, and Norbert Oswald. Orientation-guided contrastive learning for uav-view geo-localisation. In *Proceedings of the 2023 Workshop on UAVs in Multimedia: Capturing the World from a New Perspective*, page 7–11, New York, NY, USA, 2023. Association for Computing Machinery. 3, 8
- [11] Alexey Dosovitskiy, Lucas Beyer, Alexander Kolesnikov, Dirk Weissenborn, Xiaohua Zhai, Thomas Unterthiner, Mostafa Dehghani, Matthias Minderer, Georg Heigold, Sylvain Gelly, Jakob Uszkoreit, and Neil Houlsby. An Image is Worth 16x16 Words: Transformers for Image Recognition at Scale. *ArXiv*, abs/2010.11929, 2021. 8
- [12] Matthijs Douze, Alexandr Guzhva, Chengqi Deng, Jeff Johnson, Gergely Szilvasy, Pierre-Emmanuel Mazaré, Maria Lomeli, Lucas Hosseini, and Hervé Jégou. The faiss library. *arXiv*, 2024. 8
- [13] Kevin J. Gaston and Alejandro Sánchez de Miguel. Environmental impacts of artificial light at night. *Annual Review of Environment and Resources*, 47(1):373–398, 2022. 1, 3
- [14] Sergio Izquierdo and Javier Civera. Optimal transport aggregation for visual place recognition. In *IEEE Conference on Computer Vision and Pattern Recognition*, 2024. 7
- [15] Augustin Jehl, Thomas Farges, and Elisabeth Blanc. Color pictures of sprites from non-dedicated observation on board the international space station. *Journal of Geophysical Research: Space Physics*, 118(1):454–461, 2013. 1, 3
- [16] Hervé Jégou, Matthijs Douze, and Cordelia Schmid. Product quantization for nearest neighbor search. *IEEE Trans. Pattern Anal. Mach. Intell.*, 33(1):117–128, 2011. 1
- [17] Nikhil Keetha, Avneesh Mishra, Jay Karhade, Krishna Murthy Jatavallabhula, Sebastian Scherer, Madhava Krishna, and Sourav Garg. Anyloc: Towards universal visual place recognition. *arXiv*, 2023. 3, 7, 8
- [18] Shishen Li, Cuiwei Liu, Huaijun Qiu, and Zhaokui Li. A transformer-based adaptive semantic aggregation method for uav visual geo-localization. *arXiv preprint arXiv:2401.01574*, 2024. 3

- [19] Philipp Lindenberger, Paul-Edouard Sarlin, and Marc Pollefeys. LightGlue: Local Feature Matching at Light Speed. In *ICCV*, 2023. 4
- [20] Kyle McCleary, Swaminathan Gurumurthy, Paulo RM Fisch, Saral Tayal, Zachary Manchester, and Brandon Lucia. Vinsat: Solving the lost-in-space problem with visual-inertial navigation. In *IEEE International Conference on Robotics and Automation (ICRA)*, 2024. 3, 7, 8, 1
- [21] Kevin Musgrave, Serge Belongie, and Ser-Nam Lim. A metric learning reality check. In *Computer Vision – ECCV 2020*, pages 681–699, Cham, 2020. Springer International Publishing. 6
- [22] Kevin Musgrave, Serge J. Belongie, and Ser-Nam Lim. Pytorch metric learning. *ArXiv*, abs/2008.09164, 2020. 6
- [23] Aadil Nathani, Rishi Iyer, Annabelle Wang, Aarnav Chitari, Adele Wilson, and Hannah Norris. Observing Earth From Space: Using Astronaut Photography to Analyze Geographical Climate Patterns. In *AGU Fall Meeting Abstracts*, pages ED44C–06, 2022. 1, 3
- [24] OpenStreetMap Contributors. Zoom levels. https://wiki.openstreetmap.org/wiki/Zoom_levels, 2023. 3
- [25] Maxime Oquab, Timothée Darcet, Theo Moutakanni, Huy V. Vo, Marc Szafraniec, Vasil Khalidov, Pierre Fernandez, Daniel Haziza, Francisco Massa, Alaaeldin El-Nouby, Russell Howes, Po-Yao Huang, Hu Xu, Vasu Sharma, Shangwen Li, Wojciech Galuba, Mike Rabbat, Mido Assran, Nicolas Ballas, Gabriel Synnaeve, Ishan Misra, Herve Jegou, Julien Mairal, Patrick Labatut, Armand Joulin, and Piotr Bojanowski. Dinov2: Learning robust visual features without supervision, 2023. 7
- [26] Aaron Schirmer, Caleb Gallemore, Ting Liu, Seth Magle, Elisabeth DiNello, Humerah Ahmed, and Thomas Gilday. Mapping behaviorally relevant light pollution levels to improve urban habitat planning. *Scientific Reports*, 9, 2019. 1, 3
- [27] Liberty M. Shockley and Robert A. Bettinger. Real-time aerospace vehicle position estimation using terrestrial illumination matching. In *IEEE 8th International Workshop on Metrology for AeroSpace (MetroAeroSpace)*, 2021. 3
- [28] Mark A. Skinner, Michael Coletti, Matthew C. Voss, Tomas Svitek, John C. Lee, Kerstyn Auman, Hemanshu Patel, and Eamonn J. Moyer. Mitigating cubesat confusion: Results of in-flight technical demonstrations of candidate tracking and identification technologies. *Journal of Space Safety Engineering*, 9(3):403–409, 2022. 1
- [29] Christopher Small. Spectrometry of the urban lightscape. *Technologies*, 10(4), 2022. 1, 3
- [30] W. L. Stefanov and C. A. Evans. Data collection for disaster response from the international space station. *The International Archives of the Photogrammetry, Remote Sensing and Spatial Information Sciences*, XL-7/W3:851–855, 2015. 1, 3
- [31] Adam J. Stewart, Caleb Robinson, Isaac A. Corley, Anthony Ortiz, Juan M. Lavista Ferres, and Arindam Banerjee. TorchGeo: Deep learning with geospatial data. In *Proceedings of the 30th International Conference on Advances in Geographic Information Systems*, pages 1–12, Seattle, Washington, 2022. Association for Computing Machinery. 8
- [32] Alex Stoken and Kenton Fisher. Find my astronaut photo: Automated localization and georectification of astronaut photography. In *CVPRW*, pages 6196–6205, 2023. 2, 3, 7
- [33] Alex Stoken, Peter Ilhardt, Mark Lambert, and Kenton Fisher. (street) lights will guide you: Georeferencing nighttime astronaut photography of earth. In *Proceedings of the IEEE/CVF Conference on Computer Vision and Pattern Recognition (CVPR) Workshops*, pages 492–501, 2024. 2, 3
- [34] Miranda Straub and John A. Christian. Autonomous optical navigation for earth-observing satellites using coastline matching. In *AIAA Guidance, Navigation, and Control Conference*, 2015. 3
- [35] Xun Wang, Xintong Han, Weilin Huang, Dengke Dong, and Matthew R Scott. Multi-similarity loss with general pair weighting for deep metric learning. In *Proceedings of the IEEE Conference on Computer Vision and Pattern Recognition*, pages 5022–5030, 2019. 6
- [36] Yoav Yair, Melody Korman, Colin Price, and Eytan Stibbe. Observing lightning and transient luminous events from the international space station during ilan-es: An astronaut’s perspective. *Acta Astronautica*, 211:592–599, 2023. 1, 3
- [37] Ting Yao, Yiheng Zhang, Zhaofan Qiu, Yingwei Pan, and Tao Mei. Seco: Exploring sequence supervision for unsupervised representation learning. In *AAAI*, 2021. 8
- [38] Zhedong Zheng, Yujiao Shi, Tingyu Wang, Jun Liu, Jianwu Fang, Yunchao Wei, and Tat-seng Chua. Uavm ’23: 2023 workshop on uavs in multimedia: Capturing the world from a new perspective. In *ACM MM*, page 9715–9717, New York, NY, USA, 2023. Association for Computing Machinery. 3
- [39] Runzhe Zhu, Mingze Yang, Kaiyu Zhang, Fei Wu, Ling Yin, and Yujin Zhang. Modern backbone for efficient geolocalization. In *Proceedings of the 2023 Workshop on UAVs in Multimedia: Capturing the World from a New Perspective*, page 31–37, New York, NY, USA, 2023. Association for Computing Machinery. 3, 8

AstroLoc: Robust Space to Ground Image Localizer

Supplementary Material

7. Supplementary

In this Supplementary we provide additional information on the Lost-in-Space satellite problem (Sec. 7.1), on the Historical space imagery localization problem (Fig. 9), and finally we showcase a large number of qualitative results Sec. 7.3.

7.1. Lost-in-Space satellite problem

Overview The goal of “lost in space” is to identify the location/orbit of nanosatellites using computer vision. Existing solutions either involve bulky and expensive ($\sim 10k\$$) GPS receivers, months-long tracking via radio communications through ground stations [28] (a considerable fraction of CubeSats remain unidentified more than 250 days after launch [20]), or use the recent VINSat [20], a computer vision solution that localizes the satellite only if/when it flies above a set of predefined landmarks. With our more general approach to localization, we can instead localize the queries (collected in real time by the satellite) anywhere on Earth, without being constrained to a set of predefined locations or landmarks.

We apply AstroLoc by reformulating the task as image retrieval, using the dataset from McCleary et al. [20]. This dataset contains Sentinel-2 mosaics, which are not cloudless or seamlessly processed, leading to sharp boundaries and occasional oblique views (see Fig. 10, row 1 col 2). Though Sentinel 2 captures images nadir-facing (straight down), some images in this set (Fig. 10, row 1 col 2) appear to have been transformed to mimic oblique views. These conditions increase the challenge of this dataset. All images cover an area between 35k and 55k sqkm, meaning that our database can be built with only satellite images of zoom level 9, reducing the number of images required for worldwide coverage to just 12k. We therefore construct an image retrieval task with all 2500 images from [20] as queries, and 12k database images.

Results Tab. 4 shows AstroLoc’s superior performance in an out-of-distribution task, outperforming AnyLoc and EarthLoc by ~ 50 R@1. These gains highlight the impact of AstroLoc’s training setup improvements. Additionally, even the smaller AstroLoc-tiny model outperforms AnyLoc with only 2% of the parameters.

Embedded Use To better understand if this model could be actually used on a nanosatellite, we also provide results with a tiny version of AstroLoc, based on the smallest version of DINO-v2 and with output dimension of 512. This version achieves 36.7% R@1 and 74.5% R@100 with only 27M parameters (25% of the full AstroLoc), making it lightweight enough to fit on an embedded system in a nanosatellite. The memory required to store database features with AstroLoc-tiny is $12k \times 512 \times 4 \times 4 = 98$ MB: 12k images with 512 dimensional features, each repeated 4 times due to the test time rotation augmentation (see Sec. 5) and each element taking 4 bytes due to float32 encoding. Further memory reduction can be achieved through compression with methods like product quantization [16] for the features or by quantizing or pruning the model itself. Given the smaller memory footprint of this

model and database, it is feasible to use AstroLoc to run real time localization of nanosatellites. Combined with the state estimation techniques from [20], AstroLoc can power a fast, accurate, and low cost orbit determination solution.

7.2. Historical space imagery localization

Historical imagery of Earth from space represents a unique source of data to understand how Earth has changed over decadal time spans. Similar to photographs taken by astronauts aboard the ISS, lots of historical imagery from space, taken from the Space Shuttle, lacks localization information. Although efforts at manually localizing these photos have been made, with over 300k photos from the early days of the Space Shuttle (1980s) manually localized, we note that (1) a large number of these images still lack location information, and (2) these images are only weakly labeled with a single location of any pixel within the image, which is often noisy and does not represent its full extent.

Given these shortcomings, we seek to understand the performance of APL systems in localizing early photographs (1981-1984) from the Space Shuttle, which were originally taken with film cameras and then digitized. As such, they have different photometric characteristics from more recent photography, and are known⁷ to often require color correction (note the blue hue in many images in Fig. 9). We first precisely localize 704 images with the pipeline described in Sec. 3.1, and then compute localization results, reported in Tab. 5. We empirically find that AstroLoc achieves strong results even on these old photographs, showcasing its robustness to various types of domain changes. Comparing against performance on APL evaluation sets (Tab. 2, 3), AstroLoc has the smallest drop in recall (at all N) on the out-of-distribution historical imagery out of all methods tested.

7.3. Qualitative Results

Fig. 8, 9, 10 show qualitative AstroLoc results on astronaut photos, historical Earth from space imagery from the Space Shuttle, and satellite imagery from the McCleary[20] dataset, respectively. There are four examples in each row, with each example showing the query photo (leftmost) and the top-2 retrieval results (*i.e.* most similar, as ranked by AstroLoc). Correct predictions, defined as those that have *any* overlap with the query, are outlined in green, and incorrect predictions are outlined in red.

Failure Modes The most common failure modes are (1) in heavily forested areas (Fig. 8), which share similar visual characteristics to other areas in the same (as well as nearby) forests; (2) in coastal regions where very little land is in the image, causing many mostly water database images to be retrieved (Fig. 10, bottom right); and (3) the presence of occlusion, typically in the form of clouds (Fig. 10, many examples). Training specifically to ignore cloud regions may improve performance in the case of occlusions. Database curation, removing images with minimal landmass, can help alleviate the mostly water retrieval results. Further

⁷<https://eol.jsc.nasa.gov/FAQ/#photoQuality>

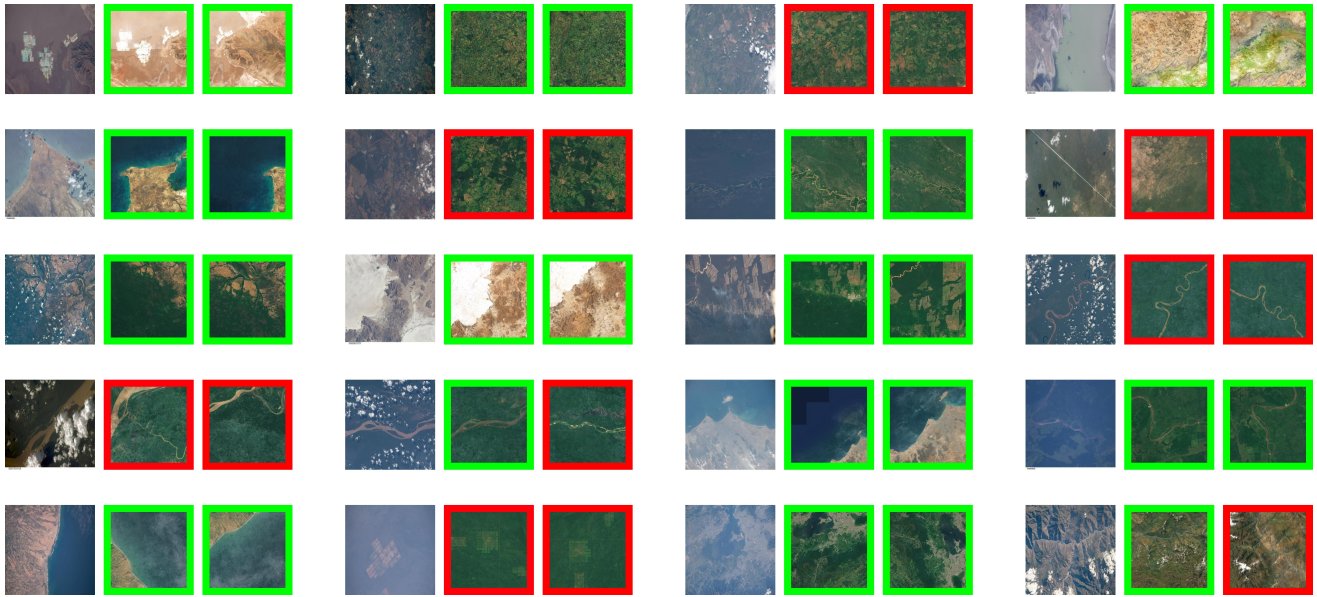


Figure 8. **Qualitative examples from the Amazon-L test set.** Each triplet shows one query and its top-2 predictions, red if wrong and green if correct.

hard negative mining may help disambiguate similar forested regions, though we note that in practice these similar (but not the same) predictions are typically filtered by a local feature-based verification method like EarthMatch [4]. Overcoming these failure modes will be explored in future work.

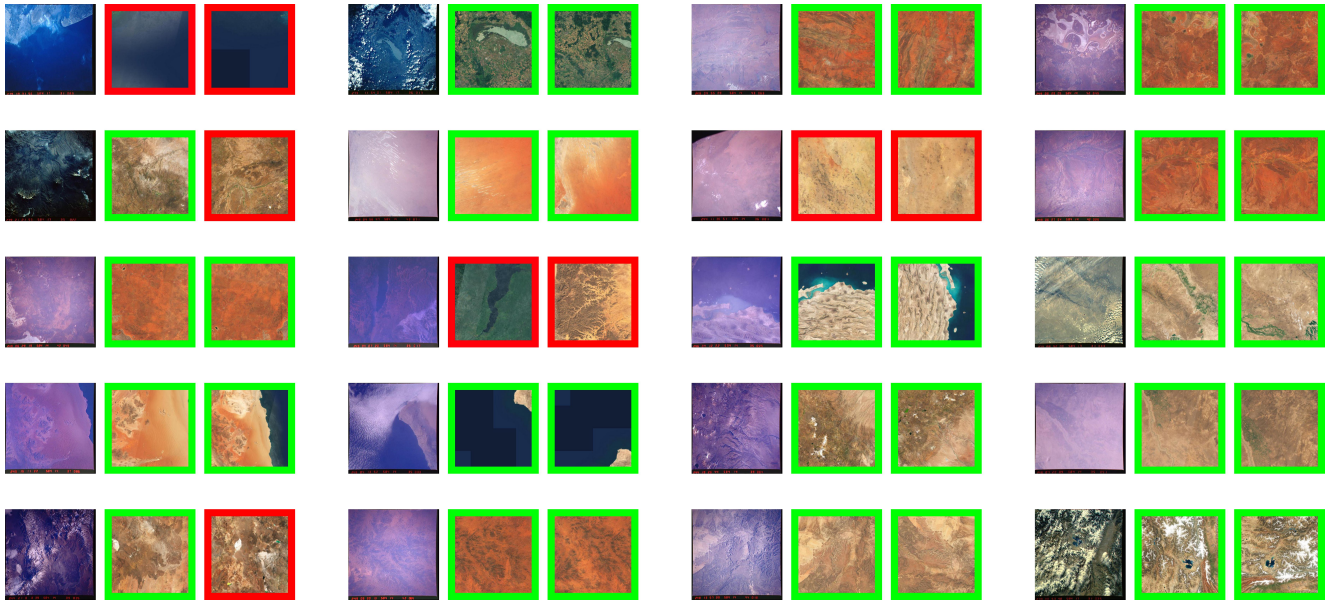


Figure 9. **Qualitative examples from the historical Space Shuttle imagery.** Each triplet shows one query and its top-2 predictions, red if wrong and green if correct. The queries were taken with analog cameras between 1981 and 1984 and then later digitized.

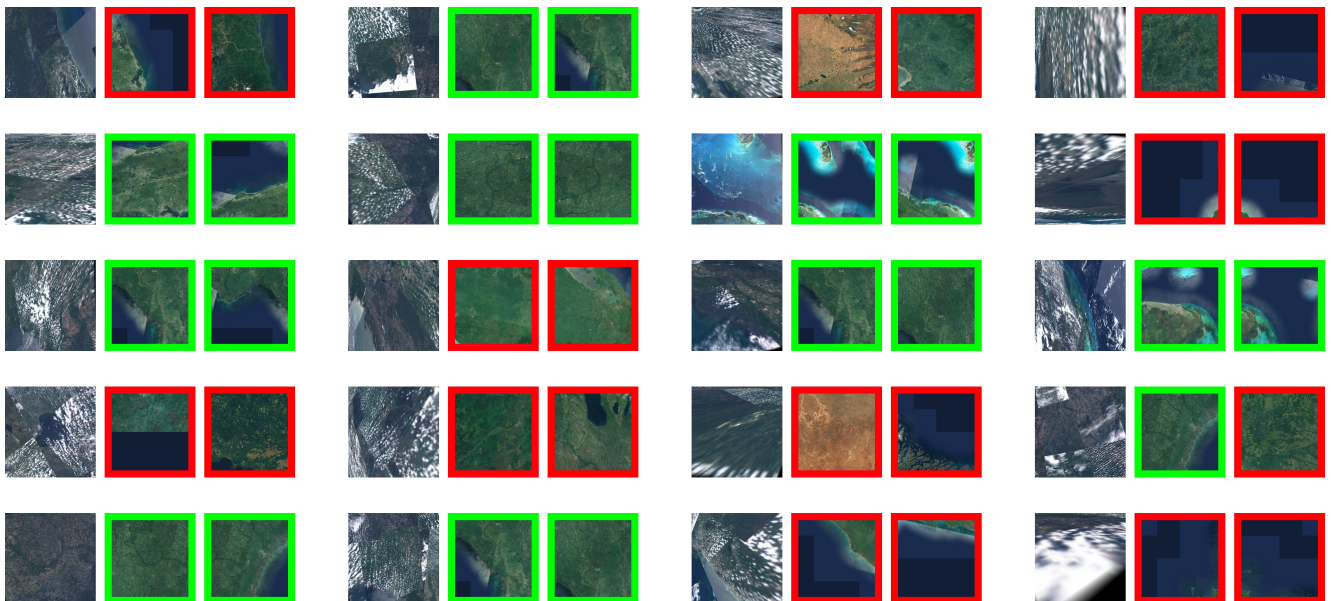


Figure 10. **Qualitative examples from the VINSat dataset [20].** Each triplet shows one query and its top-2 predictions, red if wrong and green if correct. Queries are mosaics of Sentinel 2 imagery.